# Design and Properties of Genetically Encoded Probes for Sensing Macromolecular Crowding

Boqun Liu,[1] Christoffer Åberg,[1] Floris J. van Eerden,[1] Siewert J. Marrink,[1] Bert Poolman,[1,*] and Arnold J. Boersma[1,*]

[1]Department of Biochemistry, Groningen Biomolecular Sciences and Biotechnology Institute & Zernike Institute for Advanced Materials, University of Groningen, Groningen, the Netherlands

ABSTRACT   Cells are highly crowded with proteins and polynucleotides. Any reaction that depends on the available volume can be affected by macromolecular crowding, but the effects of crowding in cells are complex and difficult to track. Here, we present a set of Förster resonance energy transfer (FRET)-based crowding-sensitive probes and investigate the role of the linker design. We investigate the sensors in vitro and in vivo and by molecular dynamics simulations. We find that in vitro all the probes can be compressed by crowding, with a magnitude that increases with the probe size, the crowder concentration, and the crowder size. We capture the role of the linker in a heuristic scaling model, and we find that compression is a function of size of the probe and volume fraction of the crowder. The FRET changes observed in *Escherichia coli* are more complicated, where FRET-increases and scaling behavior are observed solely with probes that contain the helices in the linker. The probe with the highest sensitivity to crowding in vivo yields the same macromolecular volume fractions as previously obtained from cell dry weight. The collection of new probes provides more detailed readouts on the macromolecular crowding than a single sensor.

## INTRODUCTION

The high macromolecule content in the cell, 300–400 mg/mL (1), influences the physicochemical properties in its interior. A protein in this crowded environment will endure forces due to excluded volume and nonspecific chemical interactions with the other macromolecules (2–4). Its thermodynamic activity will furthermore be affected by the solvent properties. When introducing a protein in a crowded solution, the excluded volume reduces the entropy of the system, by reducing the number of possibilities the crowders can be arranged. The entropic penalty can be relieved by reducing the volume of the introduced protein. In the cell, other interactions are able to attenuate this entropic effect, resulting in net effects that are often different from what would be predicted solely due to steric exclusion (5–12). This makes that crowding effects are unpredictable in cells, and can be overshadowed by other nonspecific interactions if the excluded volume effects are small.

To isolate excluded volume effects from other effects we developed previously a sensor for quantification of macro-

molecular crowding (13), based on Förster resonance energy transfer (FRET). The original probe consists of mCitrine (yellow fluorescent protein, YFP) and mCerulean3 (14) (cyan fluorescent protein, CFP), which form a FRET pair, and are connected by a flexible linker (Fig. 1 *A*). Upon placement in a crowded environment the probe will populate more condensed conformations, leading the FRET pair to be closer to each other. This crowding-induced compression of the whole protein is quantified by an increase in FRET efficiency between the fluorescent proteins. We validated the sensor in bacterial and mammalian cells, and observed FRET efficiencies comparable to ~20% wt/wt Ficoll in bacterial cells.

Other sensors have been developed, including a synthetic sensor based on polyethylene glycol that is compressed by macromolecular crowding (15), and a genetically encoded sensor that is based on protein-induced destabilization of an impaired YFP (16). The polyethylene glycol 10,000 (PEG)-based sensor may function via a similar mechanism to our sensor, whereas the mechanism behind the destabilization of the YFP sensor is not yet clear. Crowding can also be inferred from diffusion measurements, among other methods (17), but these are strongly dependent on other parameters such as confinement, viscosity, and nonspecific attractive interactions.

Given the multiplicity of parameters that act on a crowding sensor, we argued that a set of sensors would yield a more
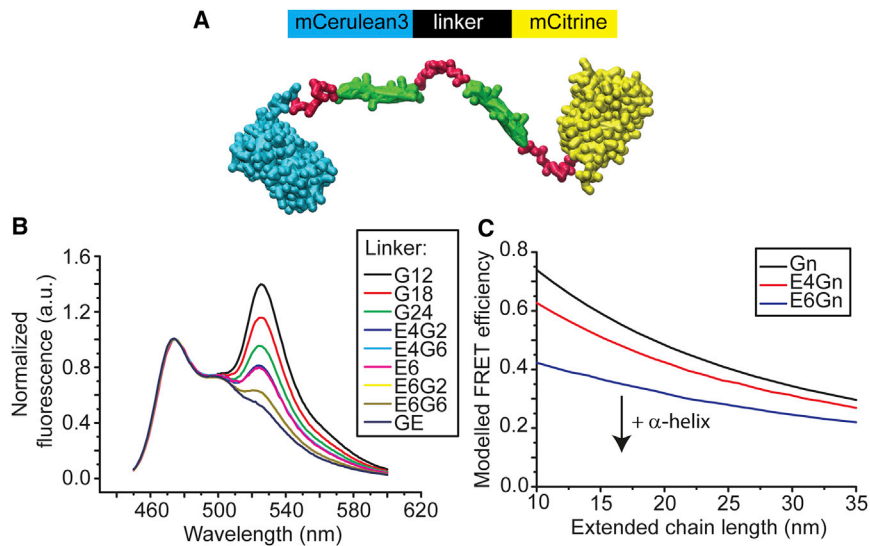
FIGURE 1 Characterization of the probes. (A) The previously developed GE probe served as a template for structural variation in the linker region. (B) Here are normalized fluorescence emission spectra of the probes in dilute buffer (10 mM NaP$_i$, 100 mM NaCl, 2 mg/mL BSA, pH 7.4), showing the range of FRET efficiencies covered. (C) The ideal chain model predicts that the FRET efficiencies of the probes in the absence of crowder decrease when $\alpha$-helices are included in the linker region, as observed experimentally (Fig. S2; Table S3). Arrow shows the direction of increasing $\alpha$-helix content. To see this figure in color, go online.

informative readout of the macromolecular crowding in cells compared to a single sensor. This is especially relevant when in-cell calibration of the sensor is prohibited, for example during time-lapse recordings. The structural simplicity of the original crowding sensor allows for a relatively straightforward design process to 1) determine the effect of structural variations in the linker on the quantification of macromolecular crowding, and 2) to uncover potential linker-induced artifacts interfering with the in-cell readouts.

We designed a set of nine probes (Table 1). We varied the linker and kept the fluorophores the same to exclude effects specific to the fluorescent proteins (18). The length of the helices and the random coil domains are varied to allow assessment if the linker flexibility and the distance between the fluorophores are affected by crowding (19,20). In here, we find that the compression of the sensors scales with probe size and volume fraction of crowder. In the cell, only probes with an $\alpha$-helix in the linker are compressed, pointing to additional contributions to the FRET besides excluded volume when the helix is absent. This set of probes

provides more detailed information on the effect of crowding in the cell than a single sensor.

## MATERIALS AND METHODS

### Plasmid preparation

The gene encoding the GE probe was obtained from GeneArt (Invitrogen GeneArt Gene Synthesis; Thermo Fisher Scientific, Waltham, MA) and subcloned into the pACYC vector in the *Sal*I and *Bam*HI sites. DNA encoding the linker region of E6G6, E6G2, E4G6, E4G2, G12, or G24 (PMK plasmid, GeneArt) was subcloned in the *Xho*I and *Sac*I of pACYC carrying the gene for the GE probe. Genes encoding the E6, GE, and the GE probe with the fluorescent proteins swapped (GES probe), all in pRSET A, were obtained from GeneArt. The gene encoding the G18 linker in the PMK plasmid (GeneArt) was subcloned in between the *Bam*HI and *Nco*I sites in the GE gene in pRSET A. To place the E6G2 and G12 genes from pACYC into pRSET A, the genes encoding E6G2 and G12 in pACYC plasmid were amplified by PCR (Forward primer: 5′-CAAAGGTGAA GAGCTCTTTACCGGTGTTGTTCCGATTC-3′ and reverse primer: 5′-TT ATTTGTACAGCTCGTCCATGCCCAGTG-3′) and digested with *Sac*I and *Eco*RI, and subsequently ligated into pRSET-A containing the GE gene. *Escherichia coli* MG1655 was transformed with the pACYC plasmids,

## TABLE 1  Probe Design and Properties

| Acronym | Linker Sequence | FRET Efficiency[a] (%) | Distance from FRET[b] (nm) |
|---|---|---|---|
| With $\alpha$-helix | | | |
| GE | —(GSG)$_6$A(EAAAK)$_6$A(GSG)$_6$A(EAAAK)$_6$A(GSG)$_6$- | 11 ± 1 | 7.6 ± 0.2 |
| E6G6 | -A(EAAAK)$_6$A(GSG)$_6$A(EAAAK)$_6$A- | 14.0 ± 0.2 | 7.3 ± 0.1 |
| E6G2 | -A(EAAAK)$_6$A(GSG)$_2$A(EAAAK)$_6$A- | 14.2 ± 0.5 | 7.3 ± 0.1 |
| E4G6 | -A(EAAAK)$_4$A(GSG)$_6$A(EAAAK)$_4$A- | 22.0 ± 0.4 | 6.7 ± 0.1 |
| E4G2 | -A(EAAAK)$_4$A(GSG)$_2$A(EAAAK)$_4$A- | 22.8 ± 0.4 | 6.6 ± 0.1 |
| E6 | -(GSG)$_6$A(EAAAK)$_6$A(GSG)$_6$- | 22.4 ± 0.5 | 6.6 ± 0.1 |
| Without $\alpha$-helix | | | |
| G24 | -(GSG)$_{24}$- | 28.4 ± 0.5 | 6.3 ± 0.1 |
| G18 | -(GSG)$_{18}$- | 34.6 ± 0.6 | 6.0 ± 0.1 |
| G12 | -(GSG)$_{12}$- | 40.9 ± 0.2 | 5.7 ± 0.1 |

[a]Efficiencies determined from the increase in mCerulean3 emission upon proteolytic cleavage as described in Materials and Methods.
[b]Distances determined from FRET efficiencies using the Förster equation. See Table S3 for more linker properties. Errors are standard deviations based on three independent repeats.

whereas *E. coli* BL21(DE3) pLysS (Promega, Madison, WI) was transformed with the pRSET A plasmids.

## Protein expression

*E. coli* BL21 (GES, GE, E6, G18, G12, or E6G2 in pRSET A) or *E. coli* MG1655 (G24, E6G6, E4G2, or E4G6 in pACYC) were grown to $OD_{600}$ 0.6 in LB medium (10 g/L tryptone, 5 g/L yeast extract, 10 g/L NaCl), and induced with 0.1 mM isopropyl $\beta$-D-1-thiogalactopyranoside (pRSET A) or 0.1% rhamnose (pACYC). After incubation at 25°C overnight, the cells were spun down at $3000 \times g$ for 30 min, resuspended in buffer A (10 mM sodium phosphate (NaP$_i$), 100 mM NaCl, 0.1 mM phenylmethyl-sulfonyl fluoride (PMSF), pH 7.4) and lysed in a tissue lyser. The lysate was cleared by centrifugation, supplemented with 10 mM imidazole, and the proteins were purified by nickel-nitrilotriacetic acid Sepharose chromatography (wash/elution buffer: 20/250 mM imidazole, 50 mM NaPi, 300 mM NaCl, pH 7.4). The constructs were further purified by Superdex 200 10/300 GL size-exclusion chromatography (Amersham Biosciences, Little Chalfont, UK) in 10 mM NaP$_i$, pH 7.4. The expression and purification were analyzed by 12% sodium dodecyl sulfate-polyacrylamide gel electrophoresis, and the bands were visualized by in-gel fluorescence and subsequent Coomassie staining. Fractions containing pure protein were aliquoted and stored at −80°C.

## Fluorometry

The crowding agent was dissolved in 10 mM NaP$_i$, 100 mM NaCl, 2 mg/mL bovine serum albumin (BSA), pH 7.4. The pH was checked after dissolution of crowding agent; crowding agents such as lysozyme and ovomucoid decreased the pH significantly and, considering the pH sensitivity of mCitrine (13), were not tested further. A 1.0-mL solution was placed in a quartz cuvette, and its fluorescence emission spectrum after excitation at 420 nm (for mCitrine and mCerulean3) and 515 nm (for mCitrine as control) were recorded at 20°C on a Fluorolog-3 (HORIBA Jobin Yvon, Edison, NJ) spectrofluorometer. Subsequently, the constructs were added, mixed by pipette, and then measured. The background spectrum from before the addition of the probe was subtracted.

## FRET efficiency determination

The fluorescence emission spectrums were recorded as before (13): 2.0 $\mu$L of Proteinase K (5.0 mg/mL in water; Sigma-Aldrich, St. Louis, MO) was added and the solution was mixed by pipette. After incubation at 20°C for 1 min, the reaction was quenched by addition of 2.0 $\mu$L PMSF (100 mM in isopropanol). Longer incubation times before quenching did not alter the spectra. The fluorescence emission spectrum was subsequently recorded. The fluorescence spectra did not change after addition of PMSF. The FRET efficiency was calculated using the following (21):

$$\text{FRET efficiency} = 1 - \frac{F_{DA}}{F_D}, \qquad (1)$$

in which $F_{DA}$ is the intensity of mCerulean3 before the cleavage, and $F_D$ is the intensity of mCerulean3 after proteolytic cleavage of the linker.

## Confocal fluorescence microscopy

Ratiometric fluorescence emission measurements of *E. coli* by scanning confocal fluorescence microscopy were carried out as reported in Boersma et al. (13). In short, *E. coli* strain BL21(DE3) pLysS containing pRSET-A with the gene encoding the probe (GE, G18, E6, G12, or E6G2) was inoculated from a glycerol stock into 10 mL of filter-sterilized MOPS minimal medium supplemented with 20 mM glucose. The culture was grown to

$OD_{600} = 0.1$–0.2. In parallel, the same *E. coli* strain with the pRSET-A plasmid with a gene encoding for a nonfluorescent protein (monomeric streptavidin), functioning as a control and background, was grown to the same $OD_{600}$. For both cultures the proteins were expressed in the absence of added inducer. The fluorescent cells were mixed with the nonfluorescent cells so as to obtain equal amounts of each cell type. The combined cells were washed by centrifugation and resuspension in MOPS minimal medium with the desired amount of NaCl, in the absence of K$_2$HPO$_4$ and glucose, to prevent adaptation of the cells. A quantity of 10 $\mu$L of this mixture was added to a coverslip modified with (3-aminopropyl) triethoxysilane (Sigma-Aldrich). For imaging, the coverslip was mounted on a laser-scanning confocal microscope (model No. LSM 710; Carl Zeiss, Oberkochen, Germany), the FRET pair was excited using a 405-mm diode laser, and the emission was split into a 450–505 nm channel and a 505–797 nm channel.

For each cell, the 505–797 nm channel (mCitrine) intensity was plotted versus the 450–505 nm channel (mCerulean3) intensity (see e.g., Fig. S9). The brightest cells were not analyzed, to minimize artifacts from intermolecular FRET, influences of high expression levels on cell contents, or incomplete maturation of the fluorescent proteins. The data was fitted to a linear equation using a least-squares approach, using the slope as the average FRET ratio.

The microscope was calibrated as described in Boersma et al. (13), briefly, as follows: a solution of the desired concentration Ficoll PM70 (20 $\mu$L, 10 mM NaP$_i$, 2 mg/mL BSA, 100 mM NaCl, pH 7.4.) was placed onto a coverslip. The microscope settings were the same as the in vivo measurement. Three pictures were taken from different locations in the same drop, and this was repeated in three different drops. The intensities were determined for the complete image. The same procedure was followed for drops without fluorescent proteins for the background measurement. The ratios were calculated by simple linear regression, using the same methodology as for the in vivo measurements. These ratios were plotted versus the ratios obtained in fluorometry, to obtain a conversion relation and hence provide direct comparison between fluorescence microscopy and fluorometry.

## Molecular dynamics simulations

The coordinates of CPF and YPF were obtained by homology modeling with SWISS-MODEL (https://swissmodel.expasy.org/) (22). For both CFP and YFP, the PDB: 4EN1 was used as a template structure. In the software PyMol (www.pymol.org) (23), the two proteins were connected by the two different linkers, creating two different sensors: GE and G18. The systems were coarse-grained and solvated using, respectively, the Martinize.py and Insane tools (24,25). NaCl was added to a concentration of ∼160 mM and on top of that, extra sodium ions were added to neutralize the systems. In the PEG systems, the concentration of PEG was ∼20% (wt/wt) (excluding the ions and the sensor); the PEG polymers consist of 136 monomers. The ubiquitin (UBQ) structure was taken from PDB: 1UBQ. In the EG and G18 systems, the concentration of ubiquitin was ∼27 and 20% (wt/wt), respectively. The composition of the various simulated systems is given in Table S1.

The systems were simulated using Martini 2.2 (http://www.cgmartini.nl/index.php/tools2/proteins-and-bilayers) (26) in conjunction with EINeDyn (26) to restrain the secondary structural motifs. For PEG, the parameterization by Lee et al. (27) was used. Test simulations indicated that the fluorescent proteins showed a high tendency to stick together, a known problem of the Martini force field (28). To increase the kinetics of the opening-closing transition of the sensor, the sensor was therefore made less sticky. This was done by decreasing the Lennard-Jones $\varepsilon$-value by 0.6 kJ/mol for all interactions between all protein beads (sensor and ubiquitin) and between the protein beads and the PEG beads. No other interactions were modified, i.e., water-water, water-protein, PEG-PEG. Note, decreasing the Lennard-Jones interactions does not result in denaturation of the fluorophores because of the use of EINeDyn. The EINeDyn bonds were only placed

on the fluorophores and on the $\alpha$-helical parts of the sensor, i.e., there were no elastic bonds between the two different $\alpha$-helices, the two fluorophores or between a fluorophore and an $\alpha$-helix.

All simulations were performed using GROMACS 4.5.5 (www.gromacs.org) (29) with the standard Martini parameters (26), at 310 K and at one bar pressure. A time step of 20 fs was used for the simulations without PEG, but a 10 fs time step had to be used in the simulations containing PEG for numerical stability. The systems were run for 15 $\mu s$ and the trajectory was saved every 1 ns. The first 1 $\mu s$ simulation time was discarded as equilibration time. This results in a total analysis time of 14 $\mu s$ per simulation.

The simulations were analyzed by calculating the FRET efficiencies. For the calculation of the FRET efficiencies, Eq. S3 was used, with $r$ as the distance between the backbone beads of the fluorophores. The Förster radius $R_0$ in Eq. S3 was calculated from $R_0 = 0.211 \times (\kappa^2 QnJ)^{1/6}$. We assumed that $R_0 = 5.4$ nm is correct for $\kappa^2 = 2/3$ (30), and calculated the remaining factor $QnJ$ based on this. Subsequently, we calculated the real $R_0$ for each conformation based on $QnJ$ being known, with the orientation factor $\kappa$ determined for each conformation from the transition dipole moments of the fluorophores as calculated by Ansbacher et al. (31), mapped to the vector between the backbone and the SC1 bead. The resulting data are presented in Table S2. From the FRET efficiencies the apparent distance between the fluorophores was calculated. Note, for a more elaborate comparison of simulation data and FRET efficiencies, see the work of Hoefling et al. (32). For the calculation of the density maps (Fig. 3 C), the tools developed by Castillo et al. (33) were used.

## RESULTS

### Design and in vitro characterization

The probes were designed in a stepwise manner with the parent GE probe serving as a starting point (Table 1). We removed the outer $(GSG)_6$ sections to decrease the probe size (the E6Gn family), and varied the length of the inner $(GSG)_n$ section, resulting in the E6G2 and E6G6 probes. We shortened the $\alpha$-helix (the E4Gn family), and again varied the internal $(GSG)_n$ section, resulting in the E4G2 and E4G6 probes. To assess whether the two helices interact with each other, we also removed one $(EAAAK)_6$ helix and a $(GSG)_6$ coil from the GE probe to obtain the E6 probe. Finally, we removed the $\alpha$-helices and varied the size of the $(GSG)_n$ linker, the Gn family.

These probes were first characterized in detail in the absence of crowders. We expressed and purified the probes and determined their properties in phosphate buffer by fluorometry (Fig. 1 B). The probes exhibit a wide range of FRET efficiencies as observed from the fluorescence emission intensities of mCitrine at 525 nm. For a direct quantification, we measured the increase in mCerulean3 emission upon proteolytic cleavage of the probes (Fig. S1), from which the FRET efficiencies and the corresponding distances $(r_0)$ between the fluorophores were determined (Table 1). The wide range of FRET efficiencies from $11 \pm 1$ to $40.9 \pm 0.2\%$ ($n = 3$) correspond to distances between the fluorophores of $7.6 \pm 0.2$ and $5.7 \pm 0.1$ nm, respectively. These average distances obtained from FRET are likely smaller than the real average distance between the fluorophores (see Table S2).

The FRET efficiencies vary with length and rigidity of the linker: The FRET efficiency of the Gn family is clearly higher than those of the E4Gn family, which, in turn, is higher than the E6Gn family (see also Fig. S2; Table S3). We can understand these observations qualitatively using simple models from polymer physics (Fig. 1 C) (Supporting Material) (34,35). These models predict that replacing part of a flexible linker with a more rigid structure will increase the probability that the two ends are far apart, explaining the lower FRET efficiencies of the helix-containing probes. Furthermore, the probability of the two ends being far apart is higher the longer the rigid part of the linker, thus explaining the difference between the E4Gn and E6Gn families. A quantitative comparison is more complicated because the persistence length is not known, it is not clear where precisely the helices end, and the fluorescent proteins also need to be considered. Nevertheless, this simple analysis suggests that the probes exhibit polymerlike behavior. These findings are in line with previous findings on random coil and $\alpha$-helix containing linkers (19,20).

### Compression relates to probe size and ficoll concentration

The effect of crowding on the probes was first studied by addition of the crowding agent Ficoll 70. In all cases, the mCitrine/mCerulean3 ratio increased with Ficoll 70 (Fig. 2 A). With the exception of G12, the ratio increased stronger with shorter linkers, which is caused by their proximity to the Förster radius (5.4 nm) (30), where the distance dependence of the FRET efficiency is highest.

We determined the distances $(r)$ between the fluorophores in all cases from the FRET efficiency (Fig. S3) and quantified the relative compression by dividing with the distance in the absence of crowder $(r_0)$. The addition of crowder changes the refractive index, inducing a small deviation in FRET efficiency (36). It would be extremely complicated to correct for the refractive index, because the intervening medium between the fluorophores contains on average less crowder, and the linker contributes to the refractive index. Assuming that the refractive index is 1.4, we underestimate crowding-induced FRET increases by 1–2%. To verify that fluorophore orientation has a negligible effect on the FRET efficiency, we constructed a probe with a circular permuted YFP. Ficoll compresses this probe in the same manner as the GE probe (Fig. S4), indicating that we only probe the distance changes. Upon comparing all the probes, we found that all probes are compressed with Ficoll, but that the larger probes also show a larger compression (Fig. 2, B and C), of up to 85% of their original size.

### Compression is related to crowder radius

Next, we determined compression of the probes with different crowding agents. We selected the GE, E6, and G18 probes, which represent the extreme and intermediate length scales and rigidities of the other probes well. BSA
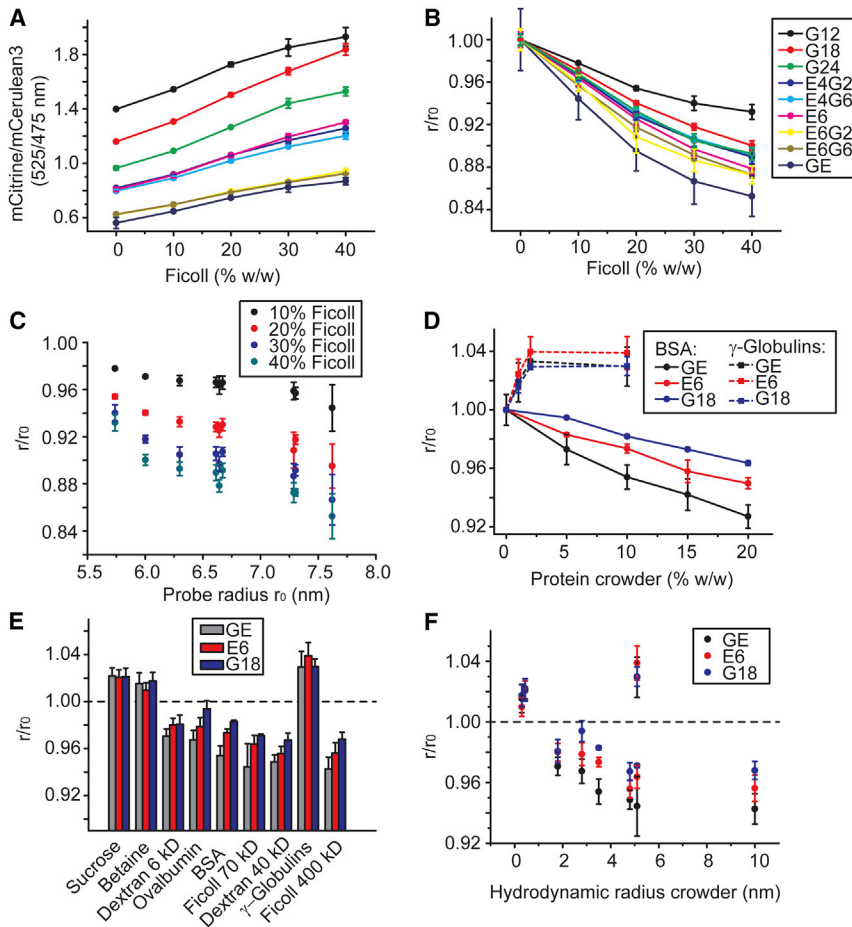
FIGURE 2 Determination of in vitro crowding-induced compression of the probes. (A) Shown here is the ratiometric fluorescence change of the probes upon titration with Ficoll 70. (B) Shown here is the compression ($r/r_0$) of the probes upon addition of Ficoll 70. The value $r_0$ is the probe radius without crowder and $r$ is the probe radius with crowder, both calculated from the FRET efficiencies. (C) Shown here is the dependence of the compression $r/r_0$ on the probe radius $r_0$, at different Ficoll concentrations; the same data as in (B). (D) Shown here is the effect of BSA and $\gamma$-Globulins at different weight % on $r/r_0$. (E) Shown here is the effect of various small molecules and macromolecular crowders, all at 10% wt/wt, on $r/r_0$. (F) Shown here are the compressions obtained for the various crowders plotted versus their hydrodynamic radius (Table S4). All experiments were performed in 10 mM NaP$_i$, 100 mM NaCl, 2 mg/mL BSA, pH 7.4. Data represent the mean ± SD of three independent experiments. To see this figure in color, go online.

induced compression of the probes with a similar trend and concentration dependence as Ficoll 70 (Fig. 2 D). The probes expanded in the presence of small amounts (1% wt/wt) of $\gamma$-Globulins, which suggests that $\gamma$-Globulins bind the probes. The probes did not expand further by addition of 10% wt/wt $\gamma$-Globulins, which could be due to saturation of binding sites, balancing excluded volume effects (9), or the decrease of attractive interactions of concentrated antibodies (37,38). We observed compression of the three probes in the presence of a variety of macromolecular crowders based on the carbohydrates Ficoll 70 and 400 kDa, Dextran 40 and 6 kDa, and the proteins BSA and ovalbumin, all at 10% wt/wt (Fig. 2 E). In all these cases, the probes compressed with a magnitude that depended on the probe and the crowder (Fig. 2 F): Compression followed probe size (GE > E6 > G18), while the dependence on the crowder hydrodynamic radius (Table S5), for fixed crowder weight %, seemed to level off at ~2–4 nm. We have previously observed the same behavior for GE in the presence of PEGs of varying weight (13). Small molecules such as sucrose and glycine betaine (each at 10% wt/wt) did not compress the probes (Fig. 2 E). The small apparent expansion of the probes of ~1–2% can at least partially be explained by the increase in refractive index upon disso-

lution of these solutes. Application of a mix of the four most abundant metabolites in *Escherichia coli* at their in vivo concentrations (potassium salts of 100 mM glutamate, 20 mM glutathione, 15 mM fructose bisphosphate, and 10 mM ATP) (39), or the application of high concentrations of salt (up to 500 mM NaCl), did not lead to an appreciable change in the FRET value (Figs. S5 and S6).

In summary, these experiments show that the probes respond to macromolecular crowding by compression, which is related to the weight percent of crowder, the probe radius, and the crowder radius. The compression is absent for small molecules and crowders with associative interactions.

## Molecular dynamics simulations confirm dependence on radii

To verify our experimental observations on the probe- and crowder-size-dependent compression, we performed coarse-grained molecular dynamics simulations (24,40). We simulated the GE and G18 probes in the absence and presence of PEG 6000 or ubiquitin (Fig. 3; Table 2), which represent a polymer- and a protein-based crowder. In experiment, we found that 20% wt/wt PEG 6000 compresses G18
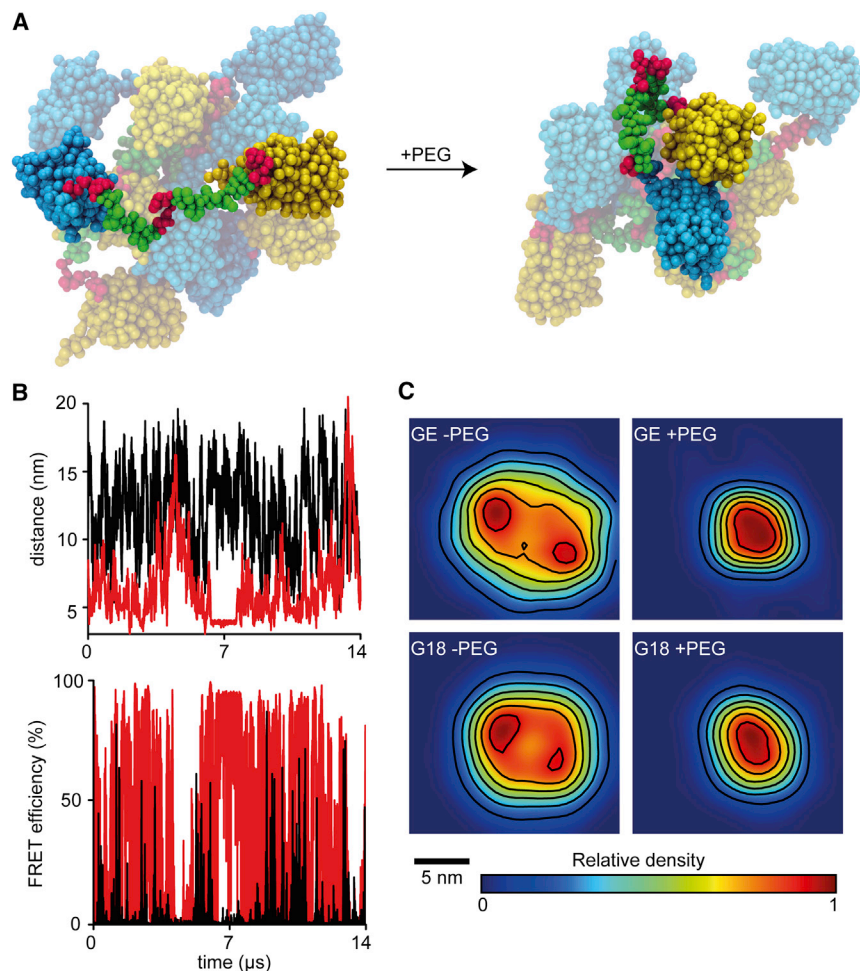
**A**



+PEG

**B**



**C**



GE -PEG

GE +PEG

G18 -PEG

G18 +PEG

Relative density

5 nm

0  1

FIGURE 3 Coarse-grained molecular dynamic simulations of the GE and G18 probes. (*A*) Shown here are snapshots of conformations of the GE probe without crowder and in the presence of PEG. For clarity, only one probe conformation is highlighted. (*B*) Shown here are time traces of the distance and calculated FRET efficiency of the GE probe with (*red*) and without (*black*) PEG. (*C*) Shown here are normalized number densities of the GE and G18 probes projected in 2D space, plotted on distance coordinates, with and without crowding with PEG. The scale bar applies to the *x*- and *y* axis. To see this figure in color, go online.

to an $r/r_0$ of ~0.88, and we previously ([13]) found for GE an $r/r_0$ of ~0.80. The simulations showed qualitative agreement with these experimental results: in both cases the addition of PEG resulted in compression of the probes, as was clearly apparent from the densities ([Fig. 3](#) *C*), leading to higher FRET efficiencies. The compression $r/r_0$ obtained from the simulations was ~0.60 for GE, and ~0.71 for G18, which confirmed the probe-size dependence qualitatively. The compression in the simulations was higher than in the experiments, which may relate to the difference in timeframe or the simulation parameters. Note, due to the

**TABLE 2 FRET Efficiencies and Distances Obtained from 14 $\mu$s Molecular Dynamic Simulations**

|  | FRET Efficiency (%) | Distance from FRET (nm) |
|---|---|---|
| **GE** | | |
| No crowder | 2.7 ± 0.4 | 9.8 ± 0.2 |
| Ubiquitin | 4.3 ± 1.6 | 9.1 ± 0.5 |
| PEG 6000 | 36.6 ± 4.4 | 5.9 ± 0.2 |
| **G18** | | |
| No crowder | 13.8 ± 0.4 | 7.3 ± 0.04 |
| Ubiquitin | 18.4 ± 2.6 | 6.9 ± 0.2 |
| PEG 6000 | 54.9 ± 15.7 | 5.2 ± 0.9 |

Errors are standard errors calculated from the means of blocks of 3.5 $\mu$s.

coarse-graining of the interactions, the MD results are qualitative rather than quantitative. The behavior of the probes both with and without crowder could be described by a single population of FRET efficiencies on this timescale, albeit that in the presence of PEG both in the case of G18 and the GE probe an additional population appeared that represented one long-term event (at ~7 $\mu$s for GE in [Fig. 3](#) *B*) where the two fluorophores dimerize. Although such events could indeed occur in experiment, the average FRET in the simulations increased upon addition of PEG without this additional population in a similar manner, and hence was not required to explain compression of the probes. The addition of ubiquitin ([Table 2](#)) leads to a smaller compression of the sensor, $r/r_0$ ~0.93, which is consistent with the smaller radius of ubiquitin. These data show that crowding-induced compression can be mimicked by simulation, and that the radii dependence is also observed in the simulations.

## Probe compression in living cells depends on the linker composition

We selected five probes for in vivo assessment of probe performance. We expressed the probes in *E. coli* BL21(DE3)

and analyzed the cells in the exponential growth phase in MOPS minimal media at OD 0.1–0.2. Under these conditions, the concentration of the probes is constant over time (Fig. S7). In-gel fluorescence of lysed cells under measurement conditions show that the probes are intact (Fig. S8). The intensities of the fluorophore emissions were determined by scanning confocal microscopy after excitation of mCerulean3 at 405 nm and subsequent determination of the mCitrine/mCerulean3 emission ratio (Fig. S9). As a further control, we constructed a probe in which the mCitrine and the mCerulean3 are swapped. The swapped probe has similar fluorescent ratios as the parent GE probe (1.03 ± 0.01 vs. 1.06 ± 0.02), further confirming the presence of intact probes.

Fig. 4 A shows that the in-cell mCitrine/mCerulean3 ratios of the probes followed the same order as in vitro. We imposed osmotic upshifts by adding NaCl to the medium to test whether the probes are sensitive to crowding in cells (13). The osmotic upshift was performed in the absence of potassium and glucose to prevent (rapid) recovery of the cell volume, and the cells were measured within 10 min to prevent alterations of the proteome. Furthermore, because the probes are less sensitive to small molecules (see above), we expect that the increase in crowding will dominate the readouts. Only a small transient increase of the cytoplasmic pH from ∼7.9 to ∼8.2 will occur upon a 500 mM NaCl-induced osmotic upshift (41), and hence the pH is unlikely to influence our measurements. The osmotic upshift increased the mCitrine/mCerulean3 ratio of the helix-containing probes (E6, E6G2), similar to the increase of the GE probe we reported previously (13). The ratios of the Gn family, on the other hand, barely increase. The GE and G18 probes diffuse roughly as rapidly as GFP (Fig. S10), which diffuses without binding to slow moving cell components, showing that the difference in response between families is not due to binding to a slow diffusing cell component that alters FRET efficiency.

We calibrated the YFP/CFP ratios in cells with the ratios of purified probes in the presence of Ficoll in microscopy. Next, we relate this microscopy data to fluorometry ratios (Fig. S11). This allowed converting in-cell data to in vitro fluorescence ratios, and thereby determination of FRET efficiencies and subsequent FRET distances (Fig. 4 B). The conversion emphasizes the observed trends of Fig. 4 A: the Gn probes were much less compressed in the cell and their FRET distances are within ∼4% of the distances in dilute buffer. However, the presence of α-helices (E6, E6G2, and GE) gave rise to a significant compression of >10%. The compression relates with the helical content of the probes, described as the (EAAAK)/(GSG) ratio (Fig. 4 C). The compression did not follow the (EAAAK)/(GSG) ratio in the case of Ficoll crowding in vitro (Fig. 4 C, inset). Indeed, in the cell the E6G2 probe was more compressed than the larger GE probe, which relates to a higher (EAAAK)/(GSG) ratio of 6.0 vs. 0.67, respectively. This data shows that, contrary to the in vitro conditions, the helices in the linker region are required for the compression of this set of probes by macromolecular crowding in living cells.

## Compression follows a scaling relation

Next, we developed a description that could capture our observations. We first noticed that the in vitro compressions
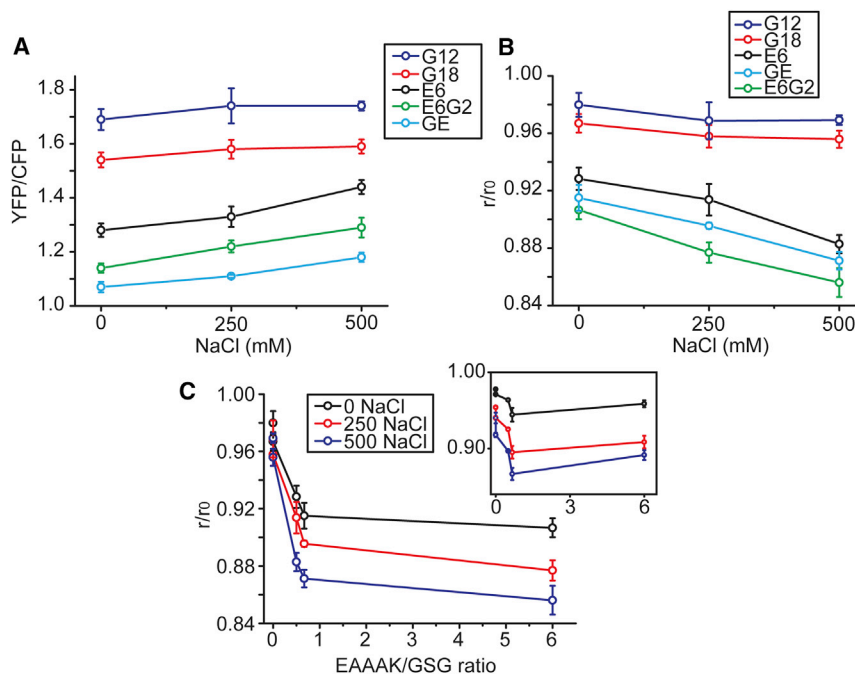


FIGURE 4 Analysis of the compression of the probes in *E. coli* cells. (A) Shown here are YFP/CFP ratios of the different probes, and change in YFP/CFP ratio upon osmotic upshift. Data represent the mean ± SD of three independent experiments. (B) Shown here are compression ($r/r_0$) of the probes in cells and effect of osmotic upshift. (C) Shown here is the dependence of the compression on the (EAAAK)/(GSG) ratio in the linker. (Inset) Given here is the in vitro dependence on the (EAAAK)/(GSG) ratio in the presence of 10 (black), 20 (red), and 30 (blue) % wt/wt Ficoll 70. Data is taken from Fig. 2 B. To see this figure in color, go online.

are qualitatively similar to those obtained for intrinsic disordered proteins in the presence of PEG, as reported by Soranno et al. (42). They explained the behavior of intrinsic disordered proteins by a renormalized Flory-Huggins theory, and hence this theory would likely fit the results of the probes used here upon adjustment of the fitting parameters. Scaled particle theory, Gaussian cloud-scaled particle theory, and Flory-Huggins theory did not fit their data, suggesting these theories would also not fit our data.

Kang et al. (43) proposed to explain the data of Soranno et al. (42) using an alternative approach. Although their approach is not microscopic, we find that it gives a surprisingly accurate description that is simple enough to use on in-cell data, something a truly microscopy description would not allow. The work of Kang et al. (43) is based on the idea of two competing length scales, namely the size of the probe in the absence of crowding, $r_0$, and the distance between crowders, $D$. If these are the only important length-scales, then the compression of the probe in the presence of crowding would fulfill a scaling relation, that is, $r/r_0 = f(r_0/D)$; $r/r_0$ depends on the ratio of the size of the probe under dilute conditions ($r_0$) to the distance between crowders ($D$). The distance between crowders can be readily estimated from the volume fraction of crowder ($\varphi$, Table S4) and the radius of the crowder ($\sigma$, Table S5) as $D \propto \sigma/\varphi^{1/3}$. We tested this ansatz on the measured compression of the probes by Ficoll 70 (Fig. 2 A), by plotting $r/r_0$ versus $(r_0/\sigma)\varphi^{1/3}$. Interestingly, the results for all probes collapse onto a single master curve (Fig. 5 A), showing that the probes are well described by this scaling relation.

The relation works well when comparing different probes, but the data no longer falls onto a single master curve when comparing different crowding agents (Fig. 5 B). However, we find, empirically, that by excluding the size of the crowder, the results again largely fall upon a single master curve (Fig. 5 C). The residual dependence on the crowder size (Fig. S12) is much smaller than that in Fig. 5 B. The heuristic master curve describes the compression of a large number of probes by several crowding agents. Importantly, we make the same observation when reanalyzing the data of Soranno et al. (42), on crowding effects on a set of intrinsically disordered proteins (Fig. S13). Thus, the same scaling relation is fulfilled by two independent experimental data sets. A potential justification for our modification of the original scaling ansatz may be that other distances than the two originally included (probe size and distance between crowders) could have a compensating effect. Notably, the crowder size is not explicitly included in the original ansatz but only enters implicitly through converting the distance between crowders to volume fraction; including this length scale explicitly could compensate for the implicit dependence from the distance between crowders. The volume fraction itself is a function of crowder size and number density and hence these parameters do influence probe compression. Furthermore, the crowder size is not constant throughout the concentration regime, as crowding agents such as Ficoll and PEG compress.

We prefer to use our modified scaling relation because of its simplicity and predictive nature. However, we stress that three important boundary conditions must be satisfied to use this empirical scaling relation as a calibration curve (Fig. 5 C; line) for interpretation of in-cell measurements, as follows: 1) compression occurs at values of $r_0\varphi^{1/3} > 2$ nm; 2) for crowder sizes <1–2 nm, the compression becomes
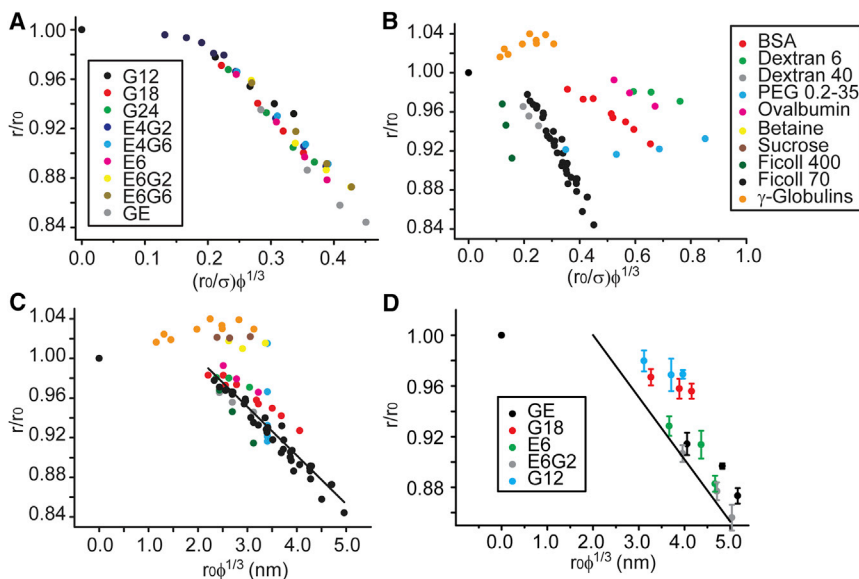


FIGURE 5 Scaling behavior of crowding-induced probe compression. (A) Compression of the probes by Ficoll 70 fulfills a scaling relation, involving the probe size, the crowding agent radius $\sigma$, (Table S5) and the crowder volume fraction $\Phi$ (determined from the partial specific volume; Table S4). Data is reproduced from Fig. 2 B, with additional data for the GE probe with 1, 2, 3, 4, 5% wt/wt Ficoll 70 to show the plateau at low volume fractions. (B) Shown here is the scaling relation of the compression for a range of crowding agents. Data is reproduced from Fig. 2 E; additionally, the PEG data of 0.2, 1.5, 4, 6, 10, 20, 35 kDa at 10% wt/wt with the GE probe is taken from Boersma et al. (13), and displayed in more detail in Fig. S12. The values for the small molecules sucrose, betaine, and PEG 0.2 kDa are off scale and not displayed. (C) Plotting the data of (B) against $r_0\varphi^{1/3}$ rather than $(r_0/\sigma)\varphi^{1/3}$ results in a collapse of the data onto a single master curve. The line is a linear fit of the probes with all crowding agents that are within the stated boundary conditions (hence excluding small molecules and γ-globulins), and excluding the data point without crowder that is not in the linear regime. (D) Given here is the comparison of in-cell compression with the modified scaling relation of Fig. 5 C, using reported volume fractions for *E. coli* (34). The line is from Fig. 5 C, and experimental data from Fig. 4 B. To see this figure in color, go online.

less; and 3) attractive interactions expand the probes. In our dataset, Ficoll 70 contributes most to the curve, and small deviations may occur when using crowders with a different radius. A range of other factors including the shape of the crowder, interactions of the crowders with itself, solvent properties, and intramolecular interactions, were apparently not strong enough to change the scaling behavior.

We next apply the relation to interpret the dependence of in-cell compression on the probe structure. We use previously determined macromolecule volume fractions inside cells from dry weight (44), and can thereby test the scaling ansatz also on in-cell data, using osmotic upshifts to increase the intracellullar crowding. We find that, even though the cytoplasm provides a vastly more complicated environment than the artificial crowding agents, the helix-containing probes (here GE, E6, and E6G2) follow the master curve measured with artificial crowders reasonably well, both without and with osmotic upshift (Fig. 5 D; Fig. S14). Especially the in-cell data for the E6G2 probe collapses very well onto the calibration line. The Gn family yields smaller compressions inside cells than predicted on the basis of the calibration line, also with osmotic upshift. This behavior can also be seen directly by comparing the lack of increase in ratio of the Gn after osmotic upshift (Fig. 4 A) versus the addition of Ficoll (Fig. 2 A). When we perform the same analysis but instead use the calibration curve to calculate the volume fraction, we see that the volume fractions reflect the (EAAAK)/(GSG) ratio in the linker (Fig. S15): the E6G2 probe yields the highest volume fractions, followed by GE and E6, whereas G18 and G12 sense the lowest volume fractions. As expected based on Fig. 5 D, good agreement with the volume fractions obtained from cell dry weight is obtained for those determined with the E6G2 probe.

Thus, compression of this set of probes follows a scaling behavior involving the size of the probe and the volume fraction of crowder, whereas in the cell, deviation from the scaling behavior occurs for linkers that do not contain the helices.

## DISCUSSION

In this article, we describe a set of FRET-based compression-sensitive protein probes. We find that 1) all probes sense macromolecular crowding, with a magnitude that depends on the probe size and crowder volume fraction (which is a function of crowder radius and concentration); and 2) the in-cell sensitivity depends on the linker composition, where only the $\alpha$-helix containing probes show an increase in FRET efficiency.

This set of probes provides more detailed information on macromolecular crowding effects. It also highlights the difference between in-cell and in vitro readouts of FRET-based probes, and warrants care when quantitatively interpreting in-cell data. We calibrate the sensors by means of osmotic upshift, and comparison with known macromolecule volume fractions and in vitro crowding. This is currently the best approach to vary the internal crowding, because other methods such as overexpression of proteins take longer and would lead to adaptation of cells. We previously showed that the volume-fraction increase, as determined with the GE probe, corresponds well to the cell volume decrease induced with an osmotic upshift (13). In vitro compression is eventually limited by the solubility of crowding agent, because the probes can be compressed continuously, and hence it is not possible to saturate the probe readout in a cell. The absence of a FRET increase with osmotic upshift for the Gn family makes it less likely that the higher FRET values in cells for the other probes are due to photophysical artifacts such as maturation or stability.

It is not directly clear from the data why the Gn family is not compressed in the cell. In lieu of direct evidence, we can hypothesize that nonspecific chemical interactions with the linker region occur, which can be prevented by the (EAAAK)n peptides. More specifically, the shielding of the peptide backbone by the helical conformation could prevent interactions between the backbone and the crowder. This would also explain the dependence on the (EAAAK)/(GSG) ratio. Additionally, the helices contain ion-paired lysines and glutamates, which are preferentially hydrated over interactions with other amino acids, and are the most common paired amino acids on cytosolic protein surfaces (45). The incorporation of paired lysines and glutamates would prevent interactions, allowing steric effects to govern the conformation. In general, the observation that in-cell behavior is different compared to in vitro crowding is not very surprising: chemical nonspecific interactions seem to dominate over the steric crowding for most reported small proteins (6–12). Hence, this is the most likely explanation, and it is remarkable that the steric compression appears to be regained by the presence of these helices. Various other explanations can be put forward, such as specific interactions with the helices or helix destabilization. However, considering the high stability of the (EAAAK) helix (46), and the absence of precedence of helix destabilization inside cells, we deem these explanations less likely. Specific autocleavage of the (EAAAK) helix has been reported (47), but we do not see new bands appearing after cell lysis, nor do we see fluorescence changes in long-term in vitro experiments. Another possibility would be repulsive charge-charge interactions of the helices with their environment. However, we do not see the same trends in vitro with the negatively charged bovine serum albumin. Small molecules such as betaine, sucrose, and PEG 0.2 kDa compensate the readout, but do so to a very small extent in the presence of crowders (data not shown), and do not allow the distinction between the families that we see in the cell.

It is highly encouraging that the E6G2 probe yields volume fractions equal to previous determined volume fractions from dry weight measurements (44). Both our

experiments and the dry-weight determination have been performed under the same conditions. However, the in-cell readout should not only depend on the volume fraction (or weight % of macromolecules), but also on how well a cytoplasm is mixed. If, for example, higher crowded regions (due to an increased affinity between the cytosolic proteins, possibly combined with size sorting by the depletion interaction) or regions with only smaller crowders exist (48,49), it may induce inhomogeneous distribution of the sensor to the less crowded regions. Inhomogeneous distribution could potentially occur under, for example, starvation conditions, or when other stresses are imposed on the cell (50–52). In these cases, the probes may indicate changes in the superstructure of the cytoplasm, especially when combined with classical volume fraction determinations from cell dry weight and probe diffusion measurements (17,44).

## CONCLUSIONS

We present a new set of crowding-sensitive probes, which we characterize extensively with a variety of methods and conditions. We show that the compression induced by crowding agents fulfills a scaling relation involving the volume fraction of crowder and the radius of the probe. In the cell, we find that (EAAAK) repeat units in the linker region of the proteins are required to compress the probes and to obtain the same scaling behavior as in vitro. The Gn family of probes serves as a control that is not compressed, whereas the E6G2 probe is compressed most in *E. coli*. We encourage the use of this set of sensors to observe possible effects other than steric repulsion, and also because the new probes provide higher sensitivity.

## SUPPORTING MATERIAL

Supporting Materials and Methods, fifteen figures, and five tables are available at http://www.biophysj.org/biophysj/supplemental/S0006-3495(17)30391-0.

## AUTHOR CONTRIBUTIONS

A.J.B. designed research. B.L., C.Å., F.J.v.E., and A.J.B. performed research. B.L., C.Å., F.J.v.E., and S.J.M. contributed new reagents/analytical tools. All authors analyzed data and wrote the paper.

## ACKNOWLEDGMENTS

## SUPPORTING CITATIONS

References (53–56) appear in the Supporting Material.

## REFERENCES

1. Zimmerman, S. B., and S. O. Trach. 1991. Estimation of macromolecule concentrations and excluded volume effects for the cytoplasm of *Escherichia coli*. *J. Mol. Biol.* 222:599–620.

2. Zhou, H. X., G. Rivas, and A. P. Minton. 2008. Macromolecular crowding and confinement: biochemical, biophysical, and potential physiological consequences. *Annu. Rev. Biophys.* 37:375–397.

3. Gnutt, D., and S. Ebbinghaus. 2016. The macromolecular crowding effect—from in vitro into the cell. *Biol. Chem.* 397:37–44.

4. Guo, M., and M. Gruebele. 2015. Spatiotemporal fluctuations of protein folding in living cells. *In* Molecular Science of Fluctuations Toward Biological Functions. M. Terazima, M. Kataoka, R. Ueoka, and Y. Okamoto, editors. Springer, Tokyo, Japan, pp. 205–219.

5. Rivas, G., and A. P. Minton. 2016. Macromolecular crowding in vitro, in vivo, and in between. *Trends Biochem. Sci.* 41:970–981.

6. Smith, A. E., L. Z. Zhou, …, G. J. Pielak. 2016. In-cell thermodynamics and a new role for protein surfaces. *Proc. Natl. Acad. Sci. USA.* 113:1725–1730.

7. Monteith, W. B., R. D. Cohen, …, G. J. Pielak. 2015. Quinary structure modulates protein stability in cells. *Proc. Natl. Acad. Sci. USA.* 112:1739–1742.

8. König, I., A. Zarrine-Afsar, …, B. Schuler. 2015. Single-molecule spectroscopy of protein conformational dynamics in live eukaryotic cells. *Nat. Methods.* 12:773–779.

9. Groen, J., D. Foschepoth, …, W. T. Huck. 2015. Associative interactions in crowded solutions of biopolymers counteract depletion effects. *J. Am. Chem. Soc.* 137:13041–13048.

10. Guzman, I., H. Gelman, …, M. Gruebele. 2014. The extracellular protein VlsE is destabilized inside cells. *J. Mol. Biol.* 426:11–20.

11. Guo, M., Y. Xu, and M. Gruebele. 2012. Temperature dependence of protein folding kinetics in living cells. *Proc. Natl. Acad. Sci. USA.* 109:17863–17867.

12. Danielsson, J., X. Mu, …, M. Oliveberg. 2015. Thermodynamics of protein destabilization in live cells. *Proc. Natl. Acad. Sci. USA.* 112:12402–12407.

13. Boersma, A. J., I. S. Zuhorn, and B. Poolman. 2015. A sensor for quantification of macromolecular crowding in living cells. *Nat. Methods.* 12:227–229.

14. Markwardt, M. L., G. J. Kremers, …, M. A. Rizzo. 2011. An improved cerulean fluorescent protein with enhanced brightness and reduced reversible photoswitching. *PLoS One.* 6:e17896.

15. Gnutt, D., M. Gao, …, S. Ebbinghaus. 2015. Excluded-volume effects in living cells. *Angew. Chem. Int. Ed. Engl.* 54:2548–2551.

16. Morikawa, T. J., H. Fujita, …, T. M. Watanabe. 2016. Dependence of fluorescent protein brightness on protein concentration in solution and enhancement of it. *Sci. Rep.* 6:22342.

17. van den Berg, J., A. J. Boersma, and B. Poolman. 2017. Microorganisms maintain crowding homeostasis. *Nat. Rev. Microbiol.* 15:309–318.

18. Dave, K., H. Gelman, …, M. Gruebele. 2016. The effect of fluorescent protein tags on phosphoglycerate kinase stability is nonadditive. *J. Phys. Chem. B.* 120:2878–2885.

19. Li, G., Z. Huang, …, X. H. Xing. 2016. Construction of a linker library with widely controllable flexibility for fusion protein design. *Appl. Microbiol. Biotechnol.* 100:215–225.

20. Evers, T. H., E. M. van Dongen, …, M. Merkx. 2006. Quantitative understanding of the energy transfer between fluorescent proteins connected via flexible peptide linkers. *Biochemistry.* 45:13183–13192.

21. Lakowicz, J. R. 2006. Principles of Fluorescence Spectroscopy, 3rd Ed. Springer, New York, p. 446.

22. Biasini, M., S. Bienert, …, T. Schwede. 2014. SWISS-MODEL: modelling protein tertiary and quaternary structure using evolutionary information. *Nucleic Acids Res.* 42:W252–W258.

23. Schrödinger.. 2010. The PyMOL Molecular Graphics System, Version 1.7.0.0. Schrödinger LLC, New York.

24. de Jong, D. H., G. Singh, ..., S. J. Marrink. 2013. Improved parameters for the Martini coarse-grained protein force field. *J. Chem. Theory Comput.* 9:687–697.

25. Wassenaar, T. A., H. I. Ingólfsson, ..., S. J. Marrink. 2015. Computational lipidomics with insane: a versatile tool for generating custom membranes for molecular simulations. *J. Chem. Theory Comput.* 11:2144–2155.

26. Periole, X., M. Cavalli, ..., M. A. Ceruso. 2009. Combining an elastic network with a coarse-grained molecular force field: structure, dynamics, and intermolecular recognition. *J. Chem. Theory Comput.* 5:2531–2543.

27. Lee, H., A. H. de Vries, ..., R. W. Pastor. 2009. A coarse-grained model for polyethylene oxide and polyethylene glycol: conformation and hydrodynamics. *J. Phys. Chem. B.* 113:13186–13194.

28. Stark, A. C., C. T. Andrews, and A. H. Elcock. 2013. Toward optimized potential functions for protein-protein interactions in aqueous solutions: osmotic second virial coefficient calculations using the MARTINI coarse-grained force field. *J. Chem. Theory Comput.* 9:4176–4185.

29. Hess, B., C. Kutzner, ..., E. Lindahl. 2008. GROMACS 4: Algorithms for highly efficient, load-balanced, and scalable molecular simulation. *J. Chem. Theory Comput.* 4:435–447.

30. Rizzo, M. A., G. Springer, ..., D. W. Piston. 2006. Optimization of pairings and detection conditions for measurement of FRET between cyan and yellow fluorescent proteins. *Microsc. Microanal.* 12:238–254.

31. Ansbacher, T., H. K. Srivastava, ..., A. Shurki. 2012. Calculation of transition dipole moment in fluorescent proteins—towards efficient energy transfer. *Phys. Chem. Chem. Phys.* 14:4109–4117.

32. Hoefling, M., N. Lima, ..., H. Grubmüller. 2011. Structural heterogeneity and quantitative FRET efficiency distributions of polyprolines through a hybrid atomistic simulation and Monte Carlo approach. *PLoS One.* 6:e19791.

33. Castillo, N., L. Monticelli, ..., D. P. Tieleman. 2013. Free energy of WALP23 dimer association in DMPC, DPPC, and DOPC bilayers. *Chem. Phys. Lipids.* 169:95–105.

34. de Gennes, P. G. 1979. Scaling Concepts in Polymer Physics. Cornell University Press, Ithaca, NY.

35. Doi, M. 1996. Introduction to Polymer Physics. Clarendon Press, Oxford, UK.

36. Knox, R. S., and H. van Amerongen. 2002. Refractive index dependence of the Förster resonance excitation transfer rate. *J. Phys. Chem. B.* 106:5289–5293.

37. Yadav, S., T. M. Laue, ..., S. J. Shire. 2012. The influence of charge distribution on self-association and viscosity behavior of monoclonal antibody solutions. *Mol. Pharm.* 9:791–802.

38. Yearley, E. J., I. E. Zarraga, ..., Y. Liu. 2013. Small-angle neutron scattering characterization of monoclonal antibody conformations and interactions at high concentrations. *Biophys. J.* 105:720–731.

39. Bennett, B. D., E. H. Kimball, ..., J. D. Rabinowitz. 2009. Absolute metabolite concentrations and implied enzyme active site occupancy in *Escherichia coli*. *Nat. Chem. Biol.* 5:593–599.

40. Ingólfsson, H. I., C. A. Lopez, ..., S. J. Marrink. 2014. The power of coarse graining in biomolecular simulations. *Wiley Interdiscip. Rev. Comput. Mol. Sci.* 4:225–248.

41. Dinnbier, U., E. Limpinsel, ..., E. P. Bakker. 1988. Transient accumulation of potassium glutamate and its replacement by trehalose during adaptation of growing cells of *Escherichia coli* K-12 to elevated sodium chloride concentrations. *Arch. Microbiol.* 150:348–357.

42. Soranno, A., I. Koenig, ..., B. Schuler. 2014. Single-molecule spectroscopy reveals polymer effects of disordered proteins in crowded environments. *Proc. Natl. Acad. Sci. USA.* 111:4874–4879.

43. Kang, H., P. A. Pincus, ..., D. Thirumalai. 2015. Effects of macromolecular crowding on the collapse of biopolymers. *Phys. Rev. Lett.* 114:068303.

44. Konopka, M. C., K. A. Sochacki, ..., J. C. Weisshaar. 2009. Cytoplasmic protein mobility in osmotically stressed *Escherichia coli*. *J. Bacteriol.* 191:231–237.

45. White, A. D., A. K. Nowinski, ..., S. Jiang. 2012. Decoding nonspecific interactions from nature. *Chem. Sci.* 3:3488–3494.

46. Marqusee, S., V. H. Robbins, and R. L. Baldwin. 1989. Unusually stable helix formation in short alanine-based peptides. *Proc. Natl. Acad. Sci. USA.* 86:5286–5290.

47. Wu, Y. J., C. Y. Fan, and Y. K. Li. 2009. Protein purification involving a unique auto-cleavage feature of a repeated EAAAK peptide. *J. Chromatogr. B Analyt. Technol. Biomed. Life Sci.* 877:4015–4021.

48. Spitzer, J., and B. Poolman. 2009. The role of biomacromolecular crowding, ionic strength, and physicochemical gradients in the complexities of life's emergence. *Microbiol. Mol. Biol. Rev.* 73:371–388.

49. Spitzer, J., and B. Poolman. 2013. How crowded is the prokaryotic cytoplasm? *FEBS Lett.* 587:2094–2098.

50. Munder, M. C., D. Midtvedt, ..., S. Alberti. 2016. A pH-driven transition of the cytoplasm from a fluid- to a solid-like state promotes entry into dormancy. *eLife.* 5:09347.

51. Joyner, R. P., J. H. Tang, ..., K. Weis. 2016. A glucose-starvation response regulates the diffusion of macromolecules. *eLife.* 5:09376.

52. Parry, B. R., I. V. Surovtsev, ..., C. Jacobs-Wagner. 2014. The bacterial cytoplasm has glass-like properties and is fluidized by metabolic activity. *Cell.* 156:183–194.

53. Mika, J. T., P. E. Schavemaker, ..., B. Poolman. 2014. Impact of osmotic stress on protein diffusion in *Lactococcus lactis*. *Mol. Microbiol.* 94:857–870.

54. Mika, J. T., V. Krasnikov, ..., B. Poolman. 2011. Evaluation of pulsed-FRAP and conventional-FRAP for determination of protein mobility in prokaryotic cells. *PLoS One.* 6:e25664.

55. Christiansen, A., Q. Wang, ..., P. Wittung-Stafshede. 2010. Factors defining effects of macromolecular crowding on protein stability: an in vitro/in silico case study using cytochrome *C*. *Biochemistry.* 49:6519–6530.

56. Mika, J. T., and B. Poolman. 2011. Macromolecule diffusion and confinement in prokaryotic cells. *Curr. Opin. Biotechnol.* 22:117–126.